ADVANCED FUNCTIONAL MATERIALS
www.afm-journal.de

Responsive Theranostic Nanoprobe for Ratiometric Photoacoustic Monitoring of Hypochlorous Acid-Mediated Inflammation in Cancer Photothermal Therapy

*Huayue Zhang, Miaomiao Wu, Firasti Agung Nugrahening Sumadi, Changkui Fu, Qingtao Meng, Mazen Alanazi, Zexi Zhang, Zhi Ping Xu, Hang Thu Ta, and Run Zhang**

Cancer detection and inflammation monitoring during photothermal therapy (PTT) enable timely cancer intervention and precise inflammation control, advancing to address inflammation-related tumor recurrence and metastasis associated with PTT. This can be achieved through real-time monitoring biomarker for cancer and inflammation, like hypochlorous acid (HOCl), a highly reactive oxygen species (hROS) in body with elevated levels in inflammation. Here, a HOCl-responsive theranostic nanoprobe is introduced, AuNRs@SiO_2-CAA for ratiometric photoacoustic (PA) cancer detection and inflammation monitoring during PTT. AuNRs@SiO_2-CAA emits PA signals at 680 and 820 nm, with only PA680 undergoing changes in the presence of HOCl, enabling precise HOCl imaging via recording changes of ratiometric PA signals (PA680/PA820). AuNRs@SiO_2-CAA exhibits high selectivity and sensitivity, with a detection limit of 0.34 µM for ratiometric PA imaging of HOCl. In vivo, it effectively detects tumor, drives PTT, and monitors inflammation during PTT by sensing HOCl. The successful development of AuNRs@SiO_2-CAA offers a novel theranostic nanoprobe system for cancer diagnosis, poised to enhance PTT through precise inflammation control.

1. Introduction

Cancer constitutes a significant global health threat with elevated mortality rates,[1] thus cancer detection and treatment have historically been primary focuses of research efforts. Recently, exploiting optical excitation and ultrasound detection benefits, photoacoustic (PA) imaging has rapidly emerged as a non-invasive imaging modality with immense potential for detecting cancer.[2] PA imaging offers outstanding tissue penetration, cost-effectiveness, absence of radiation exposure risk, and improved contrast and resolution.[3] It not only complements conventional clinical imaging modalities like magnetic resonance imaging,[4] computed tomography,[5] and ultrasound[6] but also addresses the limitations of fluorescence (FL) imaging, which suffers from deteriorating image quality with deeper tissue penetration.[7] Major PA imaging approaches entail significant accumulation of PA contrast agents at cancer sites through enhanced permeability and retention (EPR) effects.[2c,8] PA responsive probes that can be activated by cancer biomarkers have emerged as promising avenues for sensitive cancer detection.[9]

In cancer therapy, phototherapy, primarily comprising photodynamic therapy (PDT) and photothermal therapy (PTT), has gained prominence due to its non-invasiveness and minimal drug resistance.[10] Nevertheless, therapy-induced inflammation poses a significant obstacle to their effectiveness, especially for PTT.[11] PTT involves the conversion of light energy absorbed by photosensitizers into heat to destroy cancer cells locally in tumor tissue. The local temperature rise in tumor tissue induces detrimental inflammation, activating immune cells and pro-inflammatory mediators, leading to the accumulation of reactive oxygen species (ROS).[12] ROS regulate cell signaling pathways, gene expression, and participate in vital physiological processes like immune defense and apoptosis.[13] However, excessive ROS accumulation in PTT triggers abnormal responses from recruited immune cells, ultimately forming an immunosuppressive microenvironment, which leads to immune evasion and the recurrence of residual tumor cells.[14] Recently, there has been increasing interest in mitigating ROS-dominated inflammation during PTT. Strategies such as combining

---

H. Zhang, M. Wu, F. A. N. Sumadi, C. Fu, M. Alanazi, Z. Zhang, Z. P. Xu, H. T. Ta, R. Zhang
Australian Institute for Bioengineering and Nanotechnology (AIBN)
The University of Queensland
St Lucia, Queensland 4072, Australia
E-mail: r.zhang@uq.edu.au
Q. Meng
Key Laboratory of Functional Materials in Universities of Liaoning Province
School of Chemical Engineering
University of Science and Technology Liaoning
Anshan, Liaoning Province 114051, China
Z. P. Xu
Institute of Biomedical Health Technology and Engineering and Institute of Systems and Physical Biology
Shenzhen Bay Laboratory
Shenzhen 518107, China
H. T. Ta
Queensland Micro- and Nanotechnology
Griffith University
Nathan Campus, Brisbane, Queensland 4111, Australia
H. T. Ta
School of Environment and Science
Griffith University
Nathan, Queensland 4111, Australia

The ORCID identification number(s) for the author(s) of this article can be found under https://doi.org/10.1002/adfm.202414788

DOI: 10.1002/adfm.202414788

anti-inflammatory drugs with PTT[12a] or scavenging ROS[15] have been proposed to optimize PTT outcomes, showing promising results compared to PTT alone. Elucidation of dynamics of ROS-dominated inflammation development during PTT is crucial to understand the underlying mechanism of the enhanced PTT as well as to develop new therapeutics for treatment of cancers and other inflammatory disorders. Real-time monitoring of inflammation progression during PTT is essential for achieving precise inflammation control, thereby reducing the overuse of anti-inflammatory drugs and preventing cancer progression due to excessive ROS scavenging or inadequate inflammation regulation.

Hypochlorous acid (HOCl) is a highly reactive oxygen species generated through the catalytic reaction of hydrogen peroxide (H_2O_2) and chloride ions (Cl^-) by myeloperoxidase (MPO). It plays a critical role in immune defense and resistance to infections within the human body.[16] HOCl levels are intricately associated with several major diseases. They decrease in immunodeficiency disorders but significantly increase in oxidative stress-related and inflammatory diseases.[17] Thus, the development of responsive probes for monitoring HOCl levels is crucial for the diagnosis as well as treatment monitoring of different diseases, for example, acute inflammation,[18] liver injury,[19] atherosclerosis,[20] arthritis,[21] and other conditions.[22] In cancer, the abundant presence of HOCl has been extensively documented.[23] Studies indicate that photosensitizers activated by HOCl can accurately distinguish between tumor and normal cells and induce tumor cell ablation.[24] These findings underscore the potential of developing probes targeting HOCl for cancer detection. Furthermore, HOCl has been shown to play a critical role in triggering the release of neutrophil extracellular traps,[25] a key mechanism leading to immune suppression and thus affecting the efficacy of PTT. Therefore, HOCl emerges as a robust candidate for targeting biomarker to be detected for both cancer detection and inflammation monitoring during PTT.

Herein, we report the development of a responsive theranostic nanoprobe for ratiometric PA imaging of HOCl in tumor and HOCl-dominated inflammation monitoring during the PTT. The ratiometric PA nanoprobe, AuNRs@SiO_2-CAA, was developed by covalently linking an HOCl-responsive small molecular PA probe (CAA) to mesoporous silica-coated gold nanorods (AuNRs) (**Scheme 1**). As expected, AuNRs@SiO_2-CAA exhibited strong PA signals at 680 nm and 820 nm, attributed to CAA and AuNRs, respectively. Upon increasing concentration of HOCl, the rapid reaction between CAA and HOCl resulted in a gradual decrease in PA680, while PA820 remained stable. Therefore, AuNRs@SiO_2-CAA can be used for in situ detection of HOCl through ratiometric PA imaging (PA680/PA820). In vivo experiments demonstrated that AuNRs@SiO_2-CAA could be effectively delivered to tumor sites for cancer detection through monitoring HOCl levels. The AuNRs in this nanoprobe facilitated efficient PTT and allowed real-time assessment of HOCl-dominated inflammation progression during PTT. Successful development of this theranostic nanoprobe offers a new tool for monitoring tumor treatment, promising for mitigating tumor recurrence and metastasis in future.

2. Results and Discussion

2.1. Design, Preparation, and Characterization of AuNRs@SiO_2-CAA

In this work, we developed an "all-in-one" responsive theranostic nanoprobe for cancer detection, treatment, and HOCl-dominated inflammation monitoring during tumor PTT. In this theranostic nanoprobe system, a small molecule dye (CAA) served as the sensing unit for HOCl detection in cancer cells and tumors. Extended π-conjugation as well as the intramolecular charge transfer (ICT) enabled CAA applicability in PA imaging.[26] AuNRs with high light absorption in near-infrared (NIR) allowed the nanoparticles for both PA imaging as a reference signal and PTT for tumor ablation.[27] As a result of the binding CAA to AuNRs, the cancer detection and PTT-triggered inflammation monitoring could be achieved by tracking the ratiometric PA signals (PA680/PA820), while the tumor treatment could be achieved by PTT through light irradiation.

The synthesis of AuNRs@SiO_2-CAA are depicted in **Figure 1**. Initially, the small molecular PA probe, CAA, designed to react effectively with HOCl, was synthesized through a one-step reaction (Figure 1a).[28] As shown in Figure 1b, CAA reacts with a minor quantity of HOCl to produce CAA-O. As the concentration of HOCl increases, CAA-O undergoes further transformation, culminating in the formation of CAA-OCl. The mass spectrometry (MS) characterization of CAA, reaction between CAA and HOCl, the intermediate CAA-O and product CAA-OCl were tracked by MS analyses in Figure S1 (Supporting Information).

Subsequently, optical properties of CAA were validated via ultraviolet-visible (UV–vis) spectroscopy. The maximum ultraviolet (UV) absorption peak of CAA is at 651 nm. The molar extinction coefficient (ϵ) of CAA was derived from Beer's law ($A = \epsilon \cdot c_{CAA} \cdot d$) and determined to be $1.5975 \times 10^4\ L \cdot mol^{-1} \cdot cm^{-1}$. CAA exhibits a broad pH adaptability range, maintaining its maximum UV absorption intensity without peak shifting within the pH range of 5–12 (Figure S2a, Supporting Information). As the concentration of HOCl increased, the absorbance of CAA at 651 nm gradually decreased (Figure S2b, Supporting Information), while ϵ concurrently dropped to $0.9901 \times 10^4\ L \cdot mol^{-1} \cdot cm^{-1}$. The decrease in absorbance (A651) could be attributed to structural changes in the CAA molecules induced by the reaction, which impact the ICT. As shown in Figure S2c (Supporting Information), after the addition of 25 µM HOCl to 30 µg mL^{-1} CAA in buffer solutions with pH values ranging from 5 to 9, the decrease in UV absorbance at 651 nm remained consistent without significant variation. This indicates that the detection capability of the CAA nanoprobe for HOCl is not affected across this pH range, making it suitable for detection in both physiological environments (pH 7.4) and the tumor microenvironment (pH 6.5). Additionally, CAA exhibited high selectivity (Figure S3a, Supporting Information) and low cytotoxicity (Figure S3b, Supporting Information). These results demonstrate that CAA can selectively detect HOCl and is suitable for in vivo applications, making it a qualified HOCl-responsive probe. Considering its maximum absorption wavelength is located near the infrared (IR) range, it has the potential for application in PA imaging.

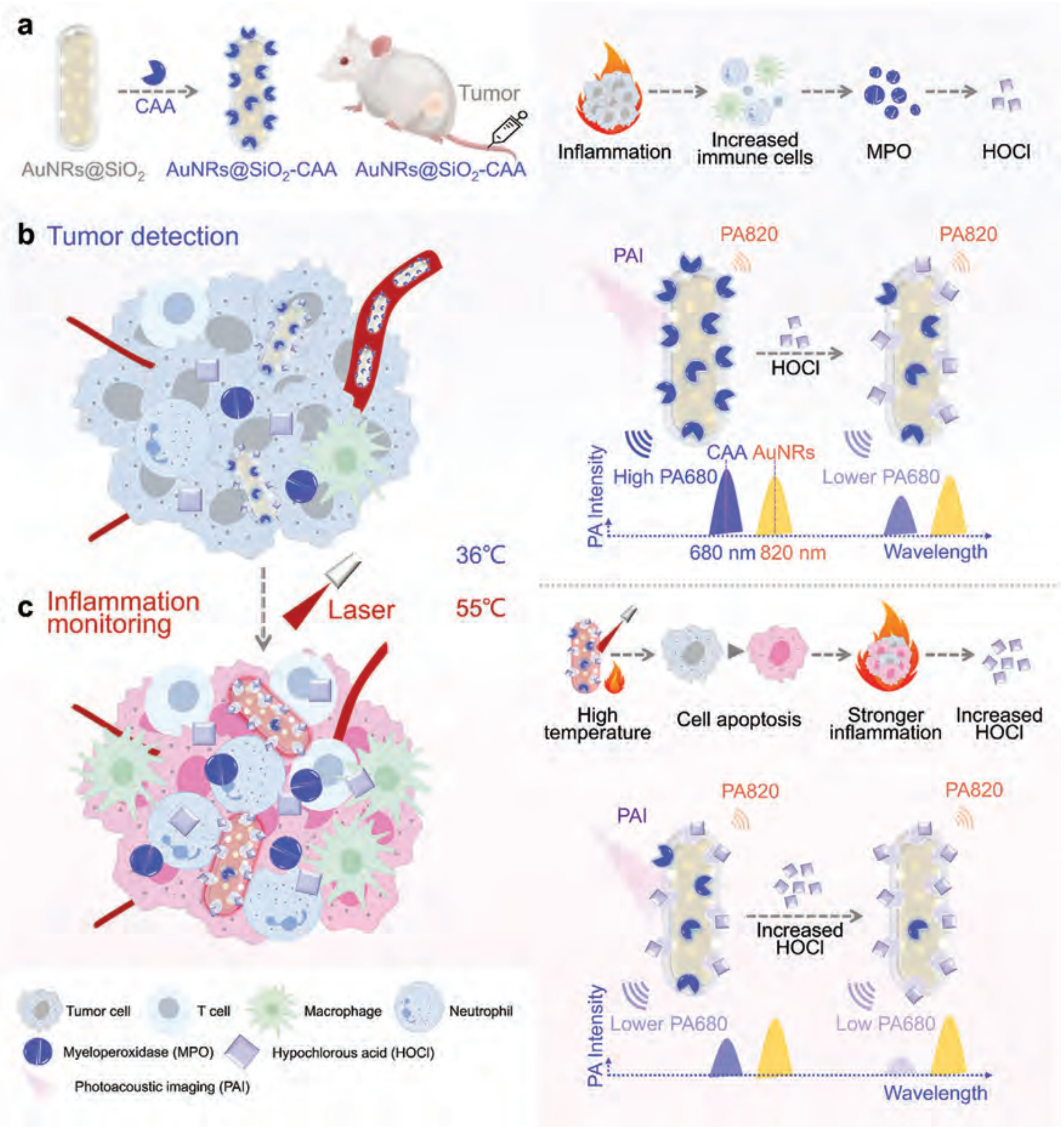

Scheme 1. Schematic illustration of the HOCl-responsive theranostic PA nanoprobe, AuNRs@SiO$_2$-CAA: a) Synthesis route of AuNRs@SiO$_2$-CAA, and its application in b) cancer detection and c) in situ monitoring of HOCl-driven inflammation progression during PTT treatment.

Next, AuNRs, acting as the second PA signal source and the photosensitizer for driving PTT, were synthesized using a seed-growth method, followed by impurity separation via centrifugation (Figure S4a, Supporting Information). The separated AuNRs solution displayed two distinct colours, brown and purplish-red (Figure S4b, Supporting Information). UV–vis verification confirmed that the brown solution contains the desired AuNRs, with a maximum absorption peak around 820 nm. It was inferred that the separated impurities, indicated by the purplish-red solution, were gold nanospheres, characterized by their color and a maximum absorption peak around 570 nm (Figure S4c, Supporting Information). Transmission electron microscopy (TEM) results illustrated that the purified AuNRs exhibited uniform rod-like structures with an aspect ratio of approximately 5.5 (Figure 1c and Figure S5, Supporting Information). The dynamic light scaterring (DLS) spectra of AuNRs showed the classical bimodal distribution (Figure S6, Supporting Information). Subsequently, the synthesis of AuNRs@SiO$_2$ was conducted. Encapsulation of AuNRs with mesoporous silica significantly reduced the toxicity of residual CTAB on the AuNRs' surface. Moreover, the abundant pores and high surface area of mesoporous silica facilitated further modification of AuNRs@SiO$_2$. TEM images (Figure S7, Supporting Information) visually demonstrated a uniform silica coating with a thickness of approximately 16 nm. The absorption peak of AuNRs@SiO$_2$ exhibits a slight redshift consistent with previous reports (Figure 1d).[29] This redshift is attributed to the formation of a silica shell, which results in an increase in the local refractive index surrounding the AuNRs.

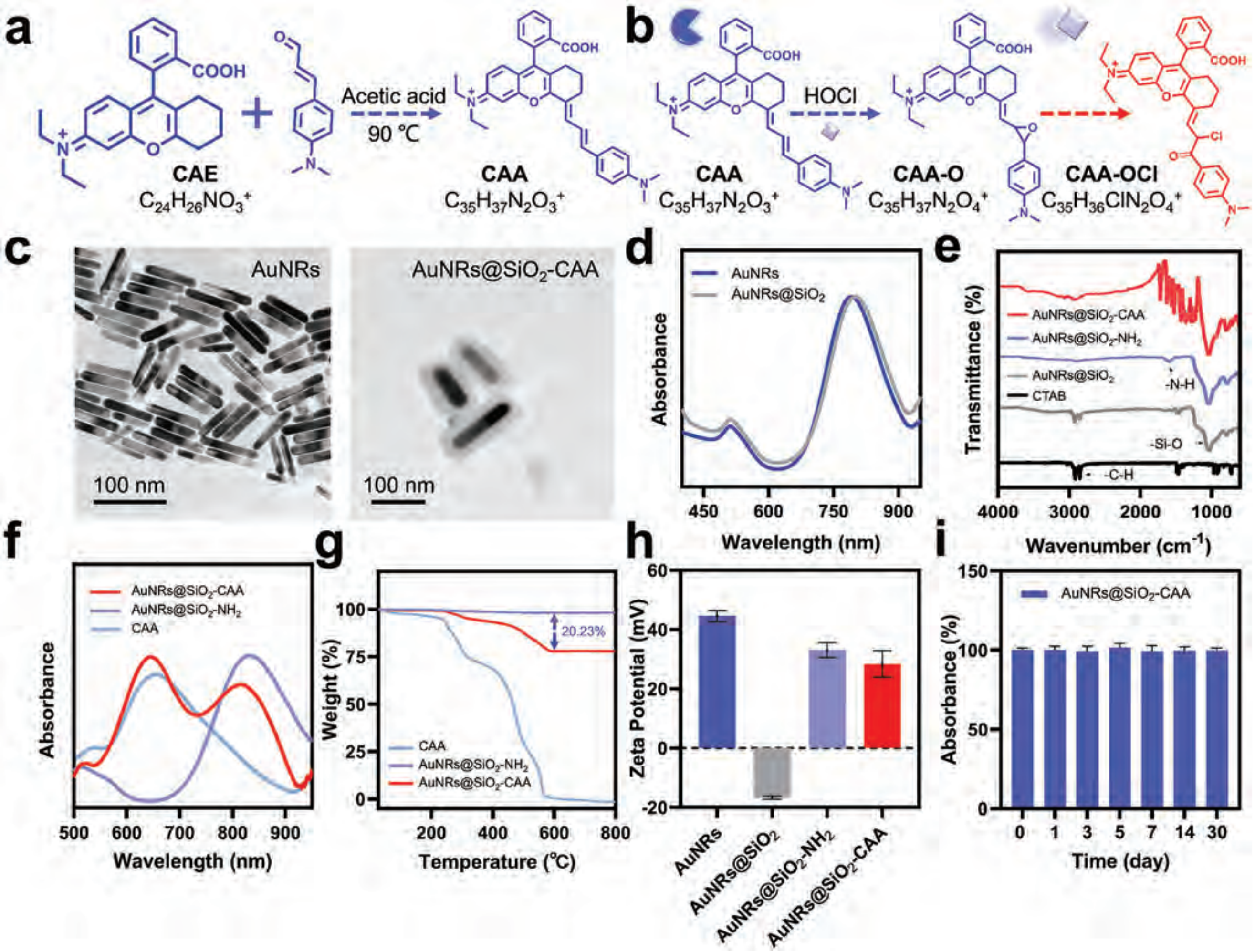

Figure 1. Preparation and characterization of AuNRs@SiO_2-CAA. a) Synthesis procedure of CAA. b) Sensing reaction mechanism between CAA and HOCl. c) Representative TEM images of AuNRs and AuNRs@SiO_2-CAA. d) UV–vis absorption spectra of AuNRs and AuNRs@SiO_2. e) FTIR spectra of CTAB, AuNRs@SiO_2, AuNRs@SiO_2-NH_2, and AuNRs@SiO_2-CAA. f) UV–vis absorption spectra of CAA, AuNRs@SiO_2-NH_2 and AuNRs@SiO_2-CAA. g) TGA curves of CAA, AuNRs@SiO_2-NH_2 and AuNRs@SiO_2-CAA. h) Zeta potentials of AuNRs, AuNRs@SiO_2, AuNRs@SiO_2-NH_2, and AuNRs@SiO_2-CAA. i) Absorption changes of AuNRs@SiO_2-CAA stored at room temperature for different time periods.

Finally, amino groups were introduced onto the surface of AuNRs@SiO_2 through grafting of APTES, facilitating the covalent linkage of CAA to AuNRs@SiO_2 via amide bonds formed between the carboxyl group of CAA and the amino groups on the silica surface, ultimately yielding AuNRs@SiO_2-CAA (Figure 1c). The appearance of characteristic peaks corresponding to -Si-O and -N-H in the Fourier transform infrared spectroscopy (FTIR) spectrum (Figure 1e) confirmed silica encapsulation and amino group incorporation. The appearance of two prominent UV absorption peaks at 651 and 820 nm confirms the successful synthesis of AuNRs@SiO_2-CAA (Figure 1f). The loading efficiency of CAA onto AuNRs@SiO_2 was elucidated through thermal gravimetric analysis (TGA). As shown in Figure 1g, the weight loss of AuNRs@SiO_2-NH_2 within the range of 30 – 700 °C can be neglected, as the melting points of gold (1064 °C) and silica (1710 °C) are significantly higher than 700 °C. Conversely, CAA underwent near-complete degradation within this temperature range. Therefore, the mass loss of AuNRs@SiO_2-CAA implies the presence of CAA therein. The loading efficiency of AuNRs@SiO_2 for CAA was approximately 20.23%. Additionally, analysis of the derivative thermogravimetric (DTG) spectra reveals that CAA within AuNRs@SiO_2-CAA retains the decomposition pattern of CAA, albeit with a slightly elevated temperature decomposition maxima. This observation suggests that the covalent attachment of CAA to AuNRs@SiO_2 enhances its thermal stability (Figure S8, Supporting Information). As illustrated in Figure 1h, the zeta potential varies across different modification steps. Upon coating AuNRs with silica, the potential shifted from 44.57 ± 1.89 mV to −16.68 ± 0.53 mV. Subsequent modification with amino groups restored a positive potential. The final product, AuNRs@SiO_2-CAA, exhibited a potential of 28.4 ± 4.37 mV, confirming the colloidal stability of the resulting nanoparticles. The long-term stability of AuNRs@SiO_2-CAA was also validated. As depicted in Figure 1i, even after 30 days of storage at room temperature, AuNRs@SiO_2-CAA maintained excellent signal stability.

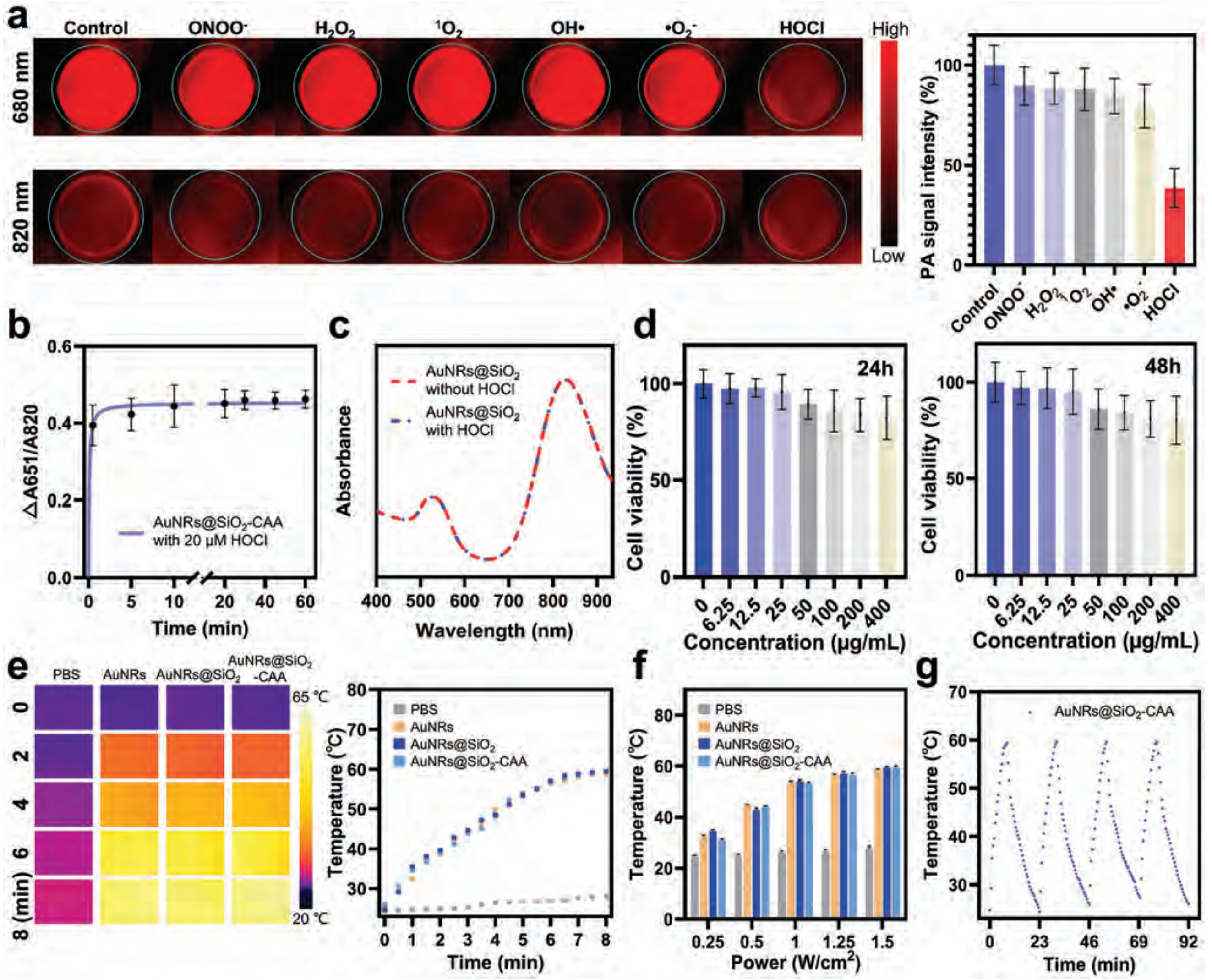

Figure 2. HOCl reactivity, biocompatibility, and photothermal properties of AuNRs@SiO$_2$-CAA. a) PA images and PA signal changes (PA680) of AuNRs@SiO$_2$-CAA (0.15 mg mL^{-1}) in the presence of different ROS (35 µM) in PBS buffer. The samples were placed in plastic tubes to conduct the PA imaging tests at 680 and 820 nm. b) Response time of AuNRs@SiO$_2$-CAA (0.15 mg mL^{-1}) to 20 µM HOCl. c) UV–vis absorption spectra of AuNRs@SiO$_2$ in the presence and absence of HOCl. d) Viability of RAW264.7 cells after adding 0–400 µg mL^{-1} AuNRs@SiO$_2$-CAA for 24 and 48 h. e) Photothermal images (PTI) and temperature increase of PBS, AuNRs, AuNRs@SiO$_2$, and AuNRs@SiO$_2$-CAA with different 808 nm laser (1.25 W cm^{-2}) exposure times. f) Temperature variations of PBS, AuNRs, AuNRs@SiO$_2$, and AuNRs@SiO$_2$-CAA under laser irradiation with different power densities. g) Temperature evolutions of AuNRs@SiO$_2$-CAA under 808 nm laser irradiation (1.25 W cm^{-2}) for 4 laser on/off cycles.

2.2. Hypochlorous Acid (HOCl)-Specific Photoacoustic (PA) Response, Biocompatibility and Photothermal Performance of AuNRs@SiO$_2$-CAA

After obtaining AuNRs@SiO$_2$-CAA, it was necessary to evaluate its functionality in detecting HOCl, driving PTT, and assessing its potential for in vivo applications. First, we confirmed the ability of AuNRs@SiO$_2$-CAA to exhibit changes in UV absorption in response to HOCl (Figure S9, Supporting Information). Subsequently, we assessed the performance of AuNRs@SiO$_2$-CAA in PA imaging. As shown in **Figure** 2a, we analyzed the PA signals of AuNRs@SiO$_2$-CAA under excitation at different wavelengths, observing strong signals at 680 and 820 nm. Upon introducing various ROS into a phosphate-buffered saline (PBS) solution containing AuNRs@SiO$_2$-CAA, only HOCl elicited a significant response, resulting in a marked decrease in PA680, while PA820 remained unchanged. Similar changes were observed in UV absorption (Figures S10,S11, Supporting Information). These findings indicate that AuNRs@SiO$_2$-CAA exhibits a responsive capability to HOCl with high selectivity. AuNRs@SiO$_2$-CAA also exhibited rapid response capability to HOCl, with the reaction nearly completing within 30 sec (Figure 2b). From Figure 2c, it can be seen that the presence of HOCl had no effect on the signal of AuNRs@SiO$_2$, indicating that the variation in probe signal intensity is solely attributed to CAA's response to HOCl. These findings collectively underscore the potential of AuNRs@SiO$_2$-CAA as a ratiometric PA probe for detecting HOCl.

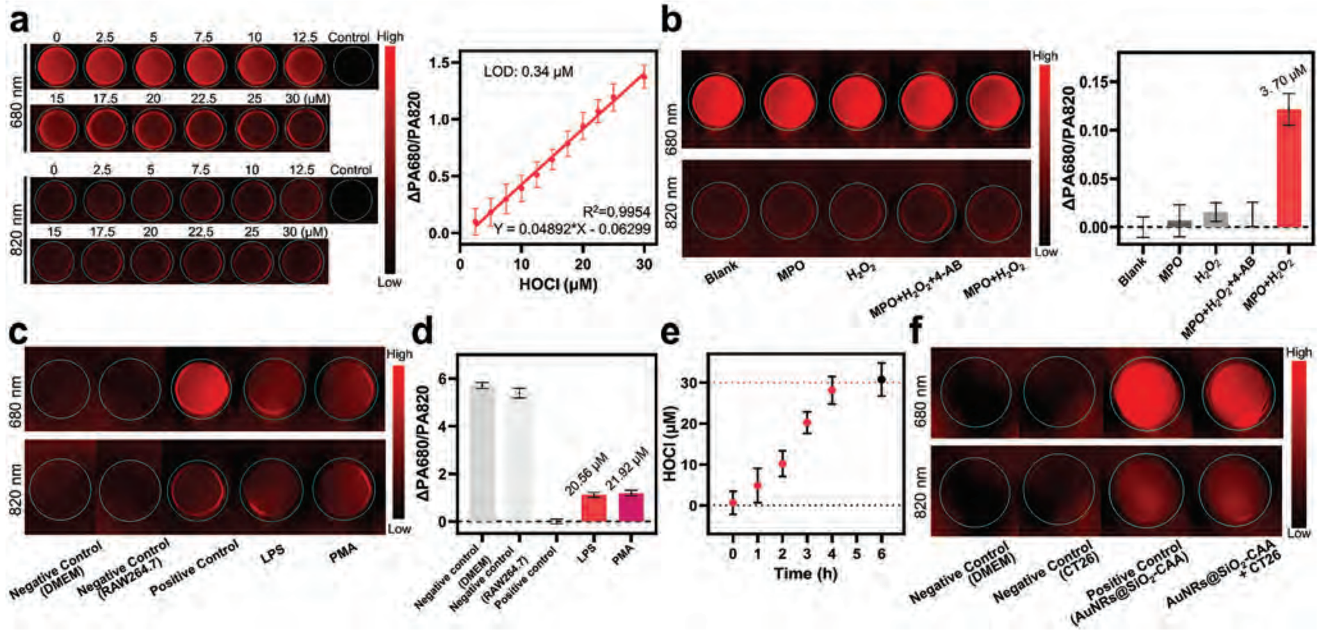

Figure 3. Detection of exogenous, MPO-generated, and endogenous HOCl by AuNRs@SiO_2-CAA. a) PA images and the curve of PA intensity ratio (ΔPA680/PA820) for AuNRs@SiO_2-CAA (150 μg mL^{-1}) in the presence of 0–30 μM HOCl. b) PA images and PA intensity ratio (ΔPA680/PA820) of AuNRs@SiO_2-CAA (150 μg mL^{-1}) upon MPO (0.05 U mL^{-1}) and H_2O_2 (8 μM) addition in PBS 7.4 in the presence of Cl^- (2 mM). c) The PA images of RAW264.7 cells incubated with AuNRs@SiO_2-CAA (150 μg mL^{-1}) in the presence or absence of LPS (1 μg mL^{-1}) or PMA (25 ng mL^{-1}) for 3 h. d) PA intensity ratio (ΔPA680/PA820) of cells shown in c) was quantified. e) Quantification of HOCl production in RAW264.7 cells incubated with LPS (1 μg mL^{-1}) over varying time periods. f) The PA images of CT26 cells incubated with AuNRs@SiO_2-CAA (150 μg mL^{-1}).

The potential for in vivo application of nanomaterials is highly determined by their biocompatibility. The cell toxicity of AuNRs@SiO_2-CAA was evaluated within RAW264.7 cells. Figure 2d shows that after 48 h of incubation with AuNRs@SiO_2-CAA at a concentration of 400 μg mL^{-1}, the survival rate of RAW264.7 cells remained high at 80.22%, confirming AuNRs@SiO_2-CAA's excellent biocompatibility. We also evaluated the photothermal performance of AuNRs@SiO_2-CAA. As depicted in Figure 2e, under 8 min of 808 nm laser irradiation, the temperature of AuNRs@SiO_2-CAA, AuNRs, and AuNRs@SiO_2 reached 59.5 °C, 58.6 °C, and 59.4 °C, respectively, whereas the temperature of PBS was only 28.1 °C. The photothermal behavior of AuNRs@SiO_2-CAA was affected by laser density, with higher laser density leading to higher temperatures. As illustrated in Figure 2f, after 8 min of laser irradiation, the temperature of AuNRs@SiO_2-CAA increased to 30.9 °C under laser irradiation at 0.25 W cm^{-2} and to 59.5 °C under laser irradiation at 1.5 W cm^{-2}. This behavior is analogous to the photothermal behavior observed for AuNRs and AuNRs@SiO_2. Furthermore, after four cycles of laser on-off process, no significant temperature decay was observed for AuNRs@SiO_2-CAA (Figure 2g), indicating its photothermal stability.

2.3. Detection of Exogenous, Myeloperoxidase (MPO)-Generated, and Endogenous HOCl by AuNRs@SiO_2-CAA

The performance of AuNRs@SiO_2-CAA in detecting HOCl from various sources was validated. To confirm the probe's response to exogenous HOCl, varying concentrations of HOCl were added to PBS containing AuNRs@SiO_2-CAA. As shown in Figure S12a (Supporting Information), the UV absorption of AuNRs@SiO_2-CAA at 651 nm gradually decreased with increasing HOCl concentration, while the UV absorption at 820 nm remained unaffected. Within the range of 0 to 35 μM, a good linear relationship was observed between ΔA651/A820 and HOCl concentration (R^2 = 0.9948), with a limit of detection (LOD) of 49.49 nM based on $3\sigma/k$. In terms of the PA signal response of AuNRs@SiO_2-CAA to HOCl, a good linear relationship was observed between ΔPA680/PA820 and HOCl concentration upon quantitative addition of 0 to 30 μM HOCl, with an LOD of 0.34 μM (**Figure 3a**). Compared to previous PA probes used for HOCl detection, AuNRs@SiO_2-CAA demonstrates competitive performance (Table S1, Supporting Information).

Subsequently, the responsiveness of AuNRs@SiO_2-CAA to HOCl generated by the MPO-catalyzed reaction between H_2O_2 and Cl^- was validated. Initially, changes in the UV–vis absorption of AuNRs@SiO_2-CAA were measured. No decrease in absorption was observed when only MPO or H_2O_2 was added. However, upon addition of both MPO and H_2O_2, a significant decrease in absorbance at 651 nm was observed, which can be inhibited by the MPO inhibitor 4-aminobenzoic acid hydrazide (4-AB) (Figure S12b, Supporting Information). From the obtained standard curve (Figure S12a, Supporting Information), the amount of HOCl produced in the $MPO/H_2O_2/Cl^-$ system was calculated to be approximately 3.32 μM. In PA imaging, a reduction in the PA signal of AuNRs@SiO_2-CAA at 680 nm was observed only in the presence of both MPO and H_2O_2. The detected amount of HOCl was approximately 3.70 μM (Figure 3b).

We next validated the performance of AuNRs@SiO_2-CAA in detecting endogenous HOCl. The macrophage cell line RAW264.7 and the colorectal cancer cell line CT26 were selected for this purpose. RAW264.7 cells, a type of macrophage, produce large amounts of ROS, including HOCl, upon stimulation with immune activators. This renders them a widely used model for validating the ability of HOCl probes to detect endogenous HOCl. The colorectal cancer cell line CT26, on the other hand, allows us to explore the ability of AuNRs@SiO_2-CAA to differentiate cancer cells by detecting HOCl. Given that the detection sensitivity of AuNRs@SiO_2-CAA to HOCl may vary with its concentration (Figure S13, Supporting Information), it is essential to generate a detection curve of HOCl in cells based on the cellular uptake behavior of AuNRs@SiO_2-CAA to ensure precise measurements. Rhodamine B (RhB) was used to label AuNRs@SiO_2-CAA, and cell uptake was characterized using flow cytometry and confocal microscopy. Figure S14a,b (Supporting Information) show the FL signal of RhB monitored by flow cytometry after incubating RhB-labeled AuNRs@SiO_2-CAA with RAW264.7 or CT26 cells for different times. The FL signal gradually shifted to the right with increasing incubation time, reaching a maximum around 9 h. Confocal microscopy showed that AuNRs@SiO_2-CAA entered the cells in a time-dependent manner, with red FL in the cytoplasm increasing over time and peaking at 9 h, consistent with flow cytometry results (Figure S14c, Supporting Information). These results demonstrated the excellent cellular accumulation ability of AuNRs@SiO_2-CAA, which is beneficial for endogenous HOCl detection. We incubated AuNRs@SiO_2-CAA with RAW264.7 cells for 9 h, washed with PBS, added different concentrations of HOCl, and detected the PA signal intensity, resulting in the HOCl detection curve of AuNRs@SiO_2-CAA in RAW264.7 cells (Figure S15a,b, Supporting Information). Lipopolysaccharide (LPS) and phorbol myristate acetate (C) were used to generate ROS in RAW264.7 cells. When incubated only with AuNRs@SiO_2-CAA, strong PA signals were observed in RAW264.7 cells at 680 and 820 nm. After incubating with PMA or LPS in the presence of AuNRs@SiO_2-CAA for 3 h, a decrease in PA680 was observed (Figure 3c). According to the detection curve (Figure S15b), the levels of HOCl produced by RAW264.7 cells were determined to be 20.56 and 21.92 µM, respectively (Figure 3d). Furthermore, the production of HOCl increased over time (Figure 3e; Figure S16, Supporting Information). We also verified the ability of AuNRs@SiO_2-CAA to detect endogenous HOCl in cancer cells. Incubation of AuNRs@SiO_2-CAA with CT26 cells resulted in a significant decrease in PA680 (Figure 3f), and further addition of HOCl led to an additional reduction in the signal (Figure S17, Supporting Information). These results confirm that AuNRs@SiO_2-CAA is potentially useful for detecting endogenous HOCl in live cells.

2.4. Monitoring of HOCl in Inflammation and Tumor Models by PA Imaging Using AuNRs@SiO_2-CAA

Inspired by the satisfactory performance of AuNRs@SiO_2-CAA in both in vitro and live cell imaging, we aimed to explore the application of AuNRs@SiO_2-CAA in living animals, with a particular focus on its performance in inflammation and cancer models. Initially, we verified the probe's capability for subcutaneous imaging and HOCl detection. Figure S18 (Supporting Information) illustrates the setup for in vivo PA imaging, where the PA signal of tissue cross-section was recorded. AuNRs@SiO_2-CAA (1.5 mg mL^{-1}, 100 µL) was administered subcutaneously into the right hind leg of mice, and PA images of the injection site were continuously acquired over a 20-min period (Figure S19a, Supporting Information). As expected, robust PA signals were detected at 680 (red-blue gradient) and 820 nm (yellow-blue gradient), persisting steadily throughout the imaging process (Figure S19b, Supporting Information). This affirmed the subcutaneous imaging capacity of AuNRs@SiO_2-CAA, alongside the absence of HOCl production in healthy mouse subcutaneous tissue. To validate AuNRs@SiO_2-CAA's capability for subcutaneous detection of exogenous HOCl, mice were sequentially injected with AuNRs@SiO_2-CAA and HOCl as the experimental group, while PBS served as the control group. Within 20 min post-injection, no significant PA signals were observed in the control group. However, notable PA signals were detected at the co-injection sites of AuNRs@SiO_2-CAA and HOCl, respectively at 680 and 820 nm (**Figure 4**a). As depicted in Figure 4b, PA680 gradually declined within the initial 10 min post-injection, then stabilized, while PA820 remained nearly constant within 20 min. This underscores the potential of AuNRs@SiO_2-CAA as a ratiometric PA probe activated by HOCl in subcutaneous tissue.

Subsequently, we induced inflammation in the back area of mice using previously reported methods involving LPS stimulation.[30] Following model establishment, AuNRs@SiO_2-CAA was injected into the inflamed area (Figure 4c). The images exhibited a gradual decrease in PA680/PA820 over 10 min (Figure 4d), indicating activation of the mouse immune system in the inflamed area, resulting in detectable levels of HOCl production. To establish a tumor-bearing mouse model, CT26 cells were implanted into the right hind leg of mice. Once the tumor reached 100 mm^3, AuNRs@SiO_2-CAA was injected around the tumor. (Figure 4e). As depicted in Figure 4f, a reduction in PA680 was observed within the initial 20 min, while PA820 remained largely unchanged, indicating the presence of HOCl at the tumor site. Over time, both PA680 and PA820 exhibited significant declines, but the ratio of PA680 to PA820 did not show a significant change. This phenomenon may be attributed to the degradation of the probe or the metabolic processes in mice. These experiments underscore the production of HOCl in both inflammation and tumor models, highlighting the potential of AuNRs@SiO_2-CAA for monitoring inflammation and tumor progression by detecting HOCl.

2.5. In Vivo Tumor Detection, Photothermal Therapy (PTT), and Real-Time Inflammation Monitoring Using AuNRs@SiO_2-CAA

Finally, we sought to apply AuNRs@SiO_2-CAA for tumor detection, treatment, and inflammation monitoring during PTT. Prior to these experiments, we investigated the accumulation of AuNRs@SiO_2-CAA at the tumor site following intravenous injection. AuNRs@SiO_2-CAA was labeled with RhB. The labeled AuNRs@SiO_2-CAA exhibited detectable fluorescence at 580 nm (Figure S20a, Supporting Information). As shown in Figure S20b (Supporting Information), CT26 tumor-bearing mice

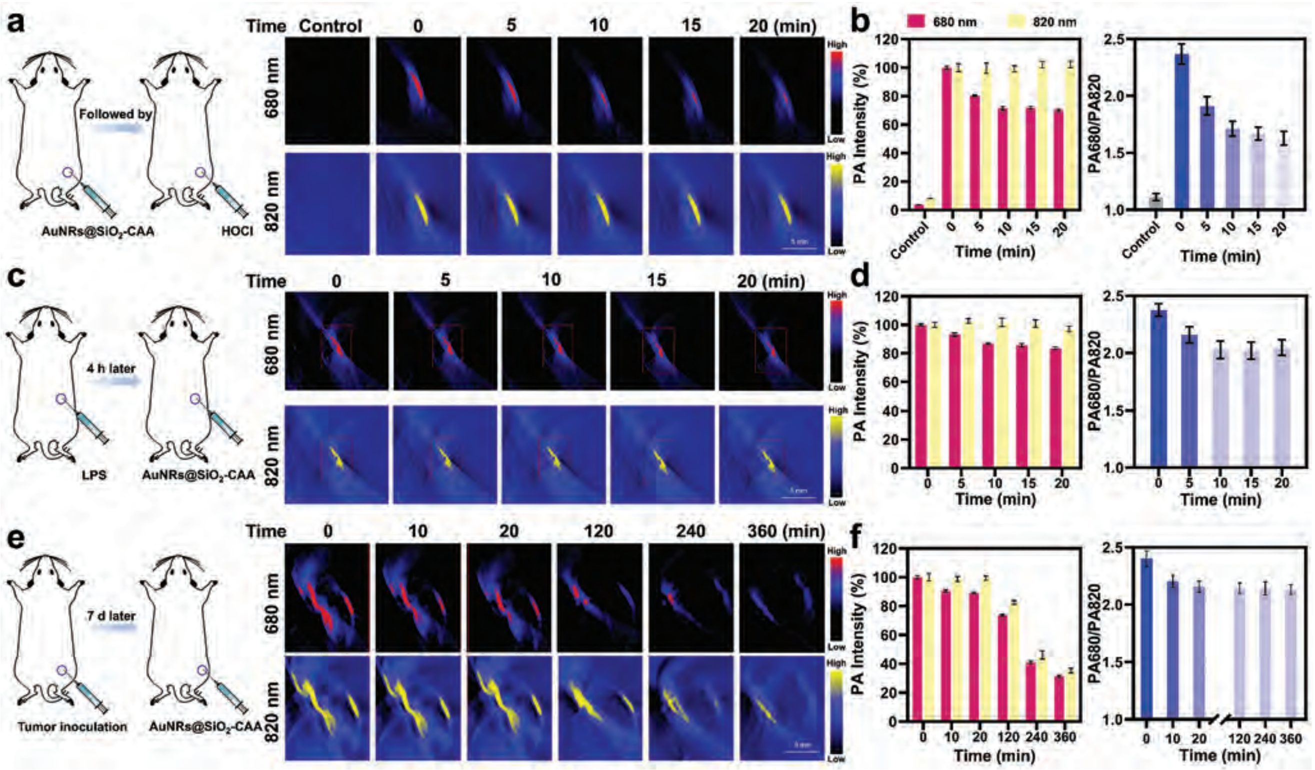

Figure 4. Monitoring of HOCl in inflammation and tumor models via PA imaging with AuNRs@SiO_2-CAA. a) AuNRs@SiO_2-CAA (1.5 mg mL^{-1}, 100 µL) was subcutaneously injected into circled area, followed by administering HOCl (100 µM, 100 µL) at the same area. PA images at 680 and 820 nm were obtained at 5, 10, 15, and 20 min. b) PA intensity and PA intensity ratio (PA680/PA820) of the injection site shown in a) was quantified. c) LPS (1 µg mL^{-1}, 100 µL) was subcutaneously injected into circled area to establish a mouse back inflammation model, followed by administering AuNRs@SiO_2-CAA (1.5 mg mL^{-1}, 100 µL) at the same area after 4 h. PA images at 680 and 820 nm were obtained at 5, 10, 15, and 20 min. d) PA intensity and PA intensity ratio (PA680/PA820) of the back inflamed region of mice shown in c) was quantified. e) PA images of subcutaneous CT26 tumors before and 10, 20, 120, 240, and 360 min after subcutaneous administration of AuNRs@SiO_2-CAA (1.5 mg mL^{-1}, 100 µL). f) PA intensity and PA intensity ratio (PA680/PA820) of the tumor region of mice shown in e) was quantified.

underwent FL imaging at various time points after intravenous injection of RhB-labeled AuNRs@SiO_2-CAA. The variation in FL signals at the tumor site indicated a time-dependent accumulation of AuNRs@SiO_2-CAA (Figure S20c, Supporting Information). Quantitative analysis of FL intensity revealed that the highest FL intensity occurred at 12 h post-injection, followed by a gradual decrease over time (Figure S20d, Supporting Information). These results indicate that AuNRs@SiO_2-CAA achieved maximal tumor accumulation at 12 h post-injection, followed by gradual clearance through systemic circulation, with most clearance achieved by 48 h. Ex vivo FL imaging of tissues harvested at 6, 12, and 24 h post-injection examined the accumulation of AuNRs@SiO_2-CAA in major organs and tumors (Figure S20c,e, Supporting Information), with relatively higher FL intensity observed in tumors harvested at 12 h post-injection. Therefore, the optimal timing for PTT was determined to be 12 h post-intravenous injection of AuNRs@SiO_2-CAA.

The experimental procedure is depicted in **Figure** 5a. Tumor models were established by subcutaneously injecting CT26 cells into the right hind leg of mice. Tumor-bearing mice, with a tumor volume reaching 100 mm^3, were randomly divided into five groups: PBS group, AuNRs@SiO_2 group, AuNRs@SiO_2-CAA group, AuNRs@SiO_2 + Laser group, and AuNRs@SiO_2-CAA + Laser group. Intravenous injections were administered twice, each with a dosage of 10 mg kg^{-1}. Laser irradiation was conducted on tumor-bearing mice 12 h after the first injection. PA imaging was performed at different time points (0, 6, 12, 24, and 48 h) following the first injection. A second injection was administered 48 h after the first injection, followed by subsequent PA imaging at different time points. Tumor volume and body weight were measured every three days throughout the entire experiment.

Figure 5b illustrates the IR thermographic images of mice during the PTT process. The local tumor temperatures of mice treated with AuNRs@SiO_2 and AuNRs@SiO_2-CAA increased to 54.9 °C and 53.3 °C, respectively, within 6 min under laser irradiation (808 nm, 1.25 W cm^{-2}). In contrast, the tumor temperature of mice treated with PBS reached only 38.4 °C (Figure S21, Supporting Information). The final tumor volumes of the five groups of mice under different treatments are visually represented in Figure 5c. Mice injected with AuNRs@SiO_2 and AuNRs@SiO_2-CAA followed by laser irradiation exhibited tumor volumes below 100 mm^3 after 21 days. In stark contrast, the tumor volumes of mice in the PBS group and those without laser treatment reached approximately 1500 mm^3 on day 21 post-treatment (Figure 5d).

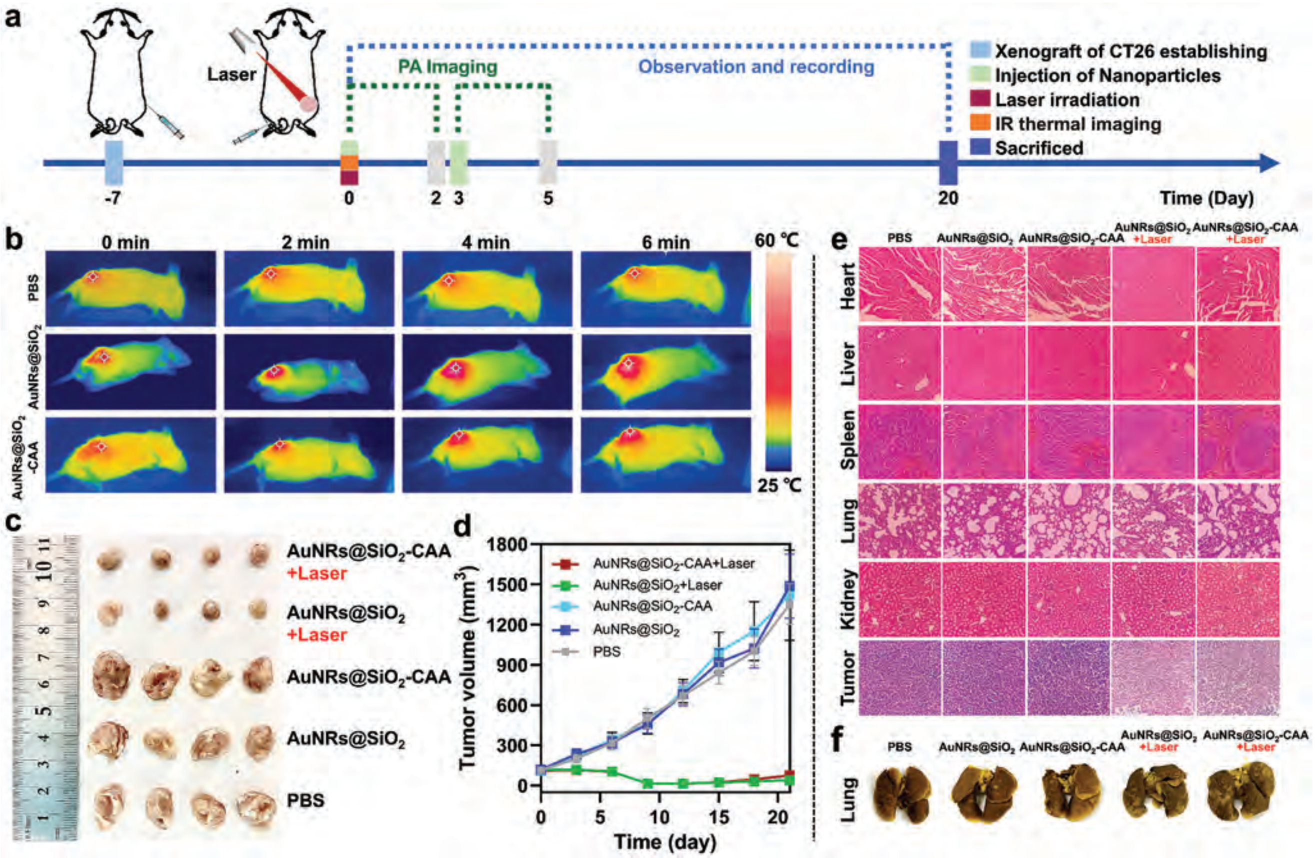

Figure 5. In vivo PTT efficacy of AuNRs@SiO_2-CAA. a) Schematic illustration of CT26 tumor xenograft establishment, administration modalities, monitoring and therapeutic timeline. b) IR thermal images of surface temperature change of tumor regions after 6 min irradiation at postinjection time of 12 h. c) Photographic images of the tumors collected from different groups of mice after treatment. d) Tumor volume of tumor-bearing mice against the treatment time. e) H&E staining of tissue sections from different groups. f) Representative images of lungs dissected from mice of different groups.

These findings demonstrate the efficacy of the PTT mediated by AuNRs@SiO_2 and AuNRs@SiO_2-CAA in tumor suppression. Hematoxylin and eosin (H&E) staining of tumor slices shown in Figure 5e indicates that laser irradiation induced significant levels of cell apoptosis and tumor tissue necrosis, further confirming the therapeutic effect of PTT. H&E staining of major organs, including the heart, liver, spleen, kidneys, and lungs, revealed no significant abnormalities or lesions in any of the groups. Additionally, no significant differences in the body weights of mice were observed among different groups throughout the entire experimental period (Figure S22, Supporting Information). These findings indicate that AuNRs@SiO_2-CAA exhibits excellent biocompatibility. Furthermore, the controllability of PTT ensures minimal damage to tissues outside the tumor site.

However, despite a significant suppression of tumor in the first 10 days post-treatment in mice subjected to PTT, there was a subsequent trend of recurrence (Figure 5d). Figure S23 (Supporting Information) demonstrates that PTT induces notable open wounds at the tumor site, requiring an extended period for scab formation. After the inoculation of CT26 cells in mice, spontaneous metastasis to other organs, such as the lungs, can occur. To evaluate the level of lung metastasis during tumor growth and PTT, lungs from different treatment groups were collected and fixed in 4% paraformaldehyde containing 10% picric acid. The appearance of white nodules in the lungs serves as an indicator of tumor presence.[31] As observed in Figure 5f, the number of nodules in mice subjected to laser irradiation did not show a significant decrease compared to other groups, indicating that PTT cannot inhibit tumor metastasis.

PA images of the mice in different groups were recorded at 680 nm and 820 nm at various time points during the experiment, represented by red-blue and yellow-blue gradients, respectively (**Figure 6**a). As shown in Figure 6b, in the AuNRs@SiO_2 and AuNRs@SiO_2 + Laser groups, PA signals were observed only at 820 nm. The signals in these two groups were very similar within the first 2 days after the initial intravenous injection, with PA820 increasing over time, peaking at 12 h postinjection, and then gradually decreasing. Given that PA820 from gold nanorods is insensitive to ROS, the observed signal increase is attributed to the EPR effect, which leads to the accumulation of the probe at the tumor site, while the subsequent decrease is due to metabolism. However, after the second injection, these two groups displayed notable differences. Despite similar trends, PA820 in the laser-treated group was consistently lower than that in the non-laser group throughout the imaging period, possibly due to laser-induced damage to the tumor interior.

In the AuNRs@SiO_2-CAA and AuNRs@SiO_2-CAA + Laser groups, PA signals were detected at both 680 nm and 820 nm

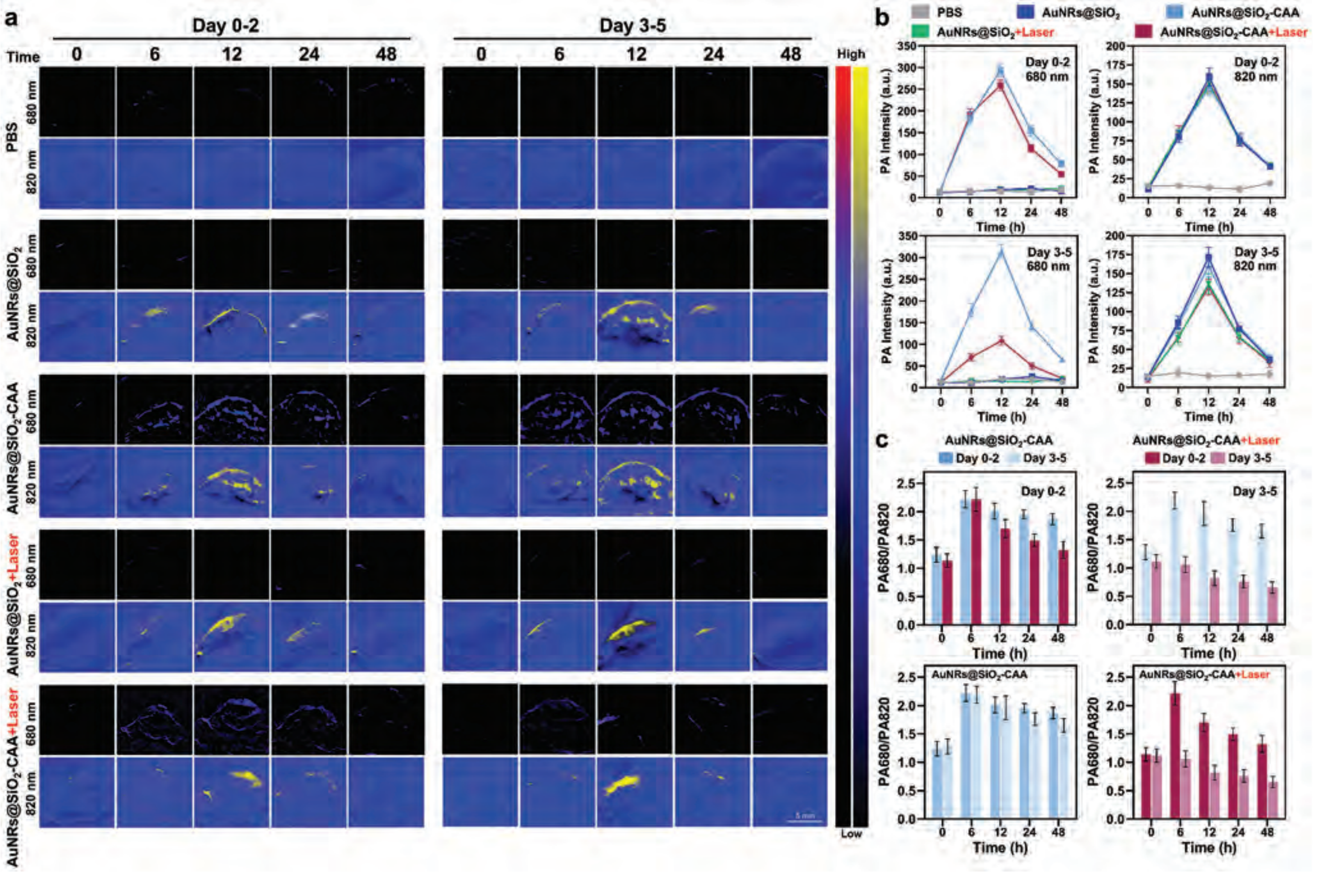

Figure 6. Real-time monitoring of HOCl generation in tumor regions using AuNRs@SiO$_2$-CAA. a) PA images of the tumor area were obtained 0–2 days and 3–5 days after PTT following intravenous injection of AuNRs@SiO$_2$-CAA (dose: 10 mg kg^{-1}). b) PA intensity and c) PA intensity ratio (PA680/PA820) of the tumor region of mice shown in a) was quantified.

(Figure 6b,c). The behavior of PA820 in these two groups resembled that of the AuNRs@SiO$_2$ and AuNRs@SiO$_2$ + Laser groups, suggesting comparable accumulation and metabolism of AuNRs@SiO$_2$ and AuNRs@SiO$_2$-CAA at the tumor site. Following the initial injection, PA680 gradually increased over time, peaking at 12 h post-injection, then declining in the AuNRs@SiO$_2$-CAA group. The decline in the PA signal ratio (PA680/PA820) suggests that the reaction between HOCl and the probe occurred simultaneously with the probe accumulation. This finding indicates the effective detection of increased HOCl by AuNRs@SiO$_2$-CAA in the tumor microenvironment. After the second injection, the continuous decrease in PA680/PA820 in the AuNRs@SiO$_2$-CAA group suggested heightened HOCl presence as the tumor expanded, highlighting AuNRs@SiO$_2$-CAA's potential in discerning tumors at varying stages. Following the initial injection, PA680/PA820 in the AuNRs@SiO$_2$-CAA + Laser group is significantly lower compared to the non-laser group, implying PTT-induced inflammation and ROS accumulation. The sustained decline in PA680/PA820 post-second injection in the AuNRs@SiO$_2$-CAA + Laser group indicated persistent PTT-induced inflammation for at least five days post-treatment. Additionally, a faint PA signal was observed in the tumors of the PBS group, likely attributable to oxy- and deoxyhemoglobin absorption.

3. Conclusion

In summary, we developed a theranostic nanoprobe for ratiometric PA cancer detection and inflammation monitoring during PTT through a HOCl response. The ratiometric PA probe, AuNRs@SiO$_2$-CAA, was synthesized by covalently linking a HOCl-responsive PA molecular probe (CAA) to mesoporous silica-coated AuNRs. CAA and AuNRs exhibit strong PA signals at 680 nm and 820 nm, respectively. In the presence of HOCl, the reaction between HOCl and CAA results in a decrease in the PA680 signal, while PA820 remains unchanged. AuNRs@SiO$_2$-CAA demonstrated excellent specificity and sensitivity, with a detection limit of 0.34 µM, surpassing most existing PA-based HOCl detection methods. At the cellular level, AuNRs@SiO$_2$-CAA effectively distinguished cancer cells and activated macrophages by quantitatively detecting elevated HOCl levels. In vivo, intravenously injected AuNRs@SiO$_2$-CAA accumulated significantly at tumor sites, with the intensity of the ratiometric PA signal correlating with tumor size. Post-PTT, AuNRs@SiO$_2$-CAA effectively reflected the severity of inflammation through monitoring HOCl levels. Our research results are expected to strengthen PTT by enabling precise inflammation monitoring during treatment through AuNRs@SiO$_2$-CAA-mediated PA imaging in the future.

4. Experimental Section

Raw Materials: All chemicals and reagents were obtained from Sigma-Aldrich unless otherwise stated. Macrophage RAW 264.7 was attained from the American Type Culture Collection (ATCC). N-nitroso-N-methylrethane-induced undifferentiated CT26 colon carcinoma cell line was obtained from Sigma-Aldrich. PBS, fetal bovine serum (FBS), Dulbecco's Modified Eagle Medium (DMEM), Trypsin-EDTA (0.25%), and 3-(4,5-dimethylthiazol-2-yl)-2,5-diphenyltetrazolium bromide (MTT) were purchased from ThermoFisher Scientific. 4-AB was obtained from Sapphire Bioscience. Milli-Q water was supplied by Milli-Q Plus System and used throughout the experiments.

Characterization: TEM images were acquired using a Hitachi HT-7700 transmission electron microscope (Japan) operated at 100 kV. The samples for TEM images were dispersed in water and then dropped on a copper grid. FTIR spectra were recorded with a Nicolet iS10 spectrometer at a resolution of 4 cm^{-1} for 32 scans to characterize surface chemical states and bonds. UV–vis absorption spectra were measured using a Shimadzu UV-2401 PC spectrometer. TGA was conducted on a Mettler Toledo TGA LF1600. The zeta potential of nanoparticles was determined using a dynamic light scattering device (DLS, Zetasizer Nano, Malvern, UK). Flow cytometry assays were conducted with a CytoFLEX flow cytometer. All living cell images were captured on a Leica SP8 confocal laser-scanning fluorescence microscope. PA imaging was performed using the MSOT InVision 256-TF Scanner.

Synthesis of CAA: In a flask containing 10 mL acetic acid, compound CAE (237.57 mg, 0.5 mmol) and 4-(dimethylamino)cinnamaldehyde (0.175 mg, 0.6 mmol) were added and the mixture was stirred at 90 °C for 6 h. After cooling down to room temperature, the solvent was removed under reduced pressure to give the crude product, that was then purified by silica gel flash chromatography using CH_2Cl_2/EtOH (150:1 to 10:1) as eluant to afford CAA (yield 80%) as green solid. NMR characterizations of CAA were presented in Figure S24 (Supporting Information). ^1H NMR (400 MHz, DMSO-d_6): δ8.20 (d, J = 8.0 Hz, 1H), 8.02 (d, J = 12.0 Hz, 1H), 7.86 (t, J = 8.0 Hz, 1H), 7.74 (t, J = 8.0 Hz, 1H), 7.62 (d, J = 8.0 Hz, 2H), 7.38 (d, J = 8.0 Hz, 1H), 7.32 (d, J = 4.0 Hz, 1H), 7.28 (d, J = 4.0 Hz, 1H), 7.20 (d, J = 4.0 Hz, 1H), 7.16 (d, J = 12.0 Hz, 1H), 6.88 (d, J = 8.0 Hz, 1H), 6.78 (d, J = 12.0 Hz, 2H), 3.63 (d, J = 4.0 Hz, 4H), 3.05 (s, 6H), 2.83 (s, 2H), 2.55 (s, 1H), 1.99 (s, 1H), 1.75 (d, J = 16.0 Hz, 2H), 1.20 (s, 6H). ^{13}C NMR (100 MHz, DMSO-d_6): δ170.79, 166.93, 157.64, 154.59, 152.32, 147.05, 133.55, 132.29, 132.06, 131.29, 130.99, 130.16, 129.53, 129.40, 124.43, 124.13, 120.56, 112.69, 112.58, 95.92, 60.22, 45.61, 25.03, 20.94, 12.96.

Synthesis of AuNRs@SiO$_2$-CAA: The AuNRs were prepared using the following protocol. In brief, 0.245 mL of 10 mM $HAuCl_4$ was added to 7.9 mL of 0.12 M CTAB solution and 1.255 mL of Milli-Q water. Then, 0.6 mL of 10 mM $NaBH_4$ (freshly prepared with cold water) was added under vigorous stirring. The seed solution was mildly stirred at 27 − 30 °C before use (light brown color). The growth solution was prepared by adding 0.47 mL of 10 mM $HAuCl_4$ to 7.9 mL of 0.12 M CTAB and 1.27 mL of Milli-Q water. Then, about 0.2 mL of 1 M HCl was added to adjust the pH value to 1.5, and the mixture was gently shaken and stirred for 5 min. Subsequently, 0.1 mL of 10 mM $AgNO_3$ solution, 0.06 mL of 100 mM ascorbic acid and 0.018 mL of seed solution were added under vigorous shaking. Finally, the resultant solution was left undisturbed at 30 °C for 12 h.

The AuNRs@SiO$_2$-CAA were prepared as follows. After centrifugation at 8500 rpm for 15 min twice, the AuNRs were re-suspended in 10 mL of Milli-Q water and 2 mL ethanol. Then, 0.1 mL of 0.1 M NaOH was added under stirring, followed by the dropwise addition of 0.03 mL of 20% TEOS every 30 min for three times. The mixture was gently stirred overnight to obtain AuNRs@SiO$_2$. Afterward, 0.03 mL of 20% (v/v) APTES in ethanol was dropwise added with incubation for 24 h to introduce amino groups to the surface of silica. After obtaining AuNRs@SiO$_2$-NH$_2$, 1 mL of 1 mg mL^{-1} CAA was prepared in 100 mM MES (pH 5–6). Then, 0.4 mg EDC was added and stirred for 15 min, followed by the addition of 0.6 mg NHS, and reacted for 15 min at room temperature. The solution pH was then adjusted to 7 before adding AuNRs@SiO$_2$-NH$_2$. Finally, the solution mixture was stirred at room temperature for 2 h and purified by centrifugation.

Synthesis of Rhodamine (RhB)-Labeled AuNRs@SiO$_2$-CAA: To label AuNRs@SiO$_2$-CAA with RhB, 120 µL of RhB isothiocyanate (concentration: 0.0719 mg mL^{-1}) was mixed with a prepared AuNRs@SiO$_2$-CAA solution (2 mg mL^{-1}). The mixture was stirred in the dark at 60 °C for 6 h. Free RhB dye was then removed by centrifugation, and the pellet was washed three times with Milli-Q water. The obtained RhB-labeled AuNRs@SiO$_2$-CAA was dispersed in PBS buffer, and its fluorescence properties were characterized using fluorescence spectroscopy with an excitation wavelength of 540 nm and an emission detection range of 550–700 nm. The sample was then stored at 4 °C in the dark for future use.

HOCl Assay: To obtain the detection standard curve of AuNRs@SiO$_2$-CAA for exogenous HOCl, various concentrations of sodium hypochlorite (NaOCl) (ranging from 0 µM to 35 µM) were added to PBS (pH 7.4) containing AuNRs@SiO$_2$-CAA (150 µg mL^{-1}). The mixture was equilibrated for 30 s before measurement. UV–vis absorption spectra from 400 to 1000 nm and PA signals at 680 nm and 820 nm were measured to plot the curves.

The assay for enzymatic HOCl generation was conducted in PBS containing 2 mM Cl^- (pH 7.40). PBS, 150 µg mL^{-1} AuNRs@SiO$_2$-CAA, and 0.05 U mL^{-1} MPO were gently mixed. After five minutes, the reaction was initiated by adding 8 µM H_2O_2. To ensure metabolite formation was dependent on both the enzyme and H_2O_2, parallel incubations were performed with the enzyme inhibitor 4-AB (5 µM), without the enzyme source, and without H_2O_2. The solutions were incubated at 37 °C for 25 min. UV–vis absorption spectra and PA signals were then measured.

The detection of endogenous HOCl using AuNRs@SiO$_2$-CAA was conducted as outlined below: RAW264.7 cells and CT26 cells were cultured in DMEM medium containing 10% (v/v) FBS, 100 U mL^{-1} penicillin, and 100 µg mL^{-1} streptomycin at 37 °C under 5% CO_2 and 95% air. For RAW264.7 cells, after 24 h of incubation, adherent cells were washed thrice with PBS buffer (pH 7.4). In the experimental group, RAW264.7 cells were incubated with AuNRs@SiO$_2$-CAA (150 µg mL^{-1}) for 9 h, washed thrice with PBS buffer (pH 7.4), then treated with LPS (1 µg mL^{-1}) or PMA (25 ng mL^{-1}) for 3 h, washed again thrice with PBS buffer (pH 7.4), and subsequently subjected to PA imaging. In the control group, RAW264.7 cells were incubated with AuNRs@SiO$_2$-CAA (150 µg mL^{-1}) for 9 h, washed thrice with PBS buffer (pH 7.4), and directly subjected to PA imaging.

For CT26 cells, after 24 h of incubation, the culture medium was removed, and the cells were washed thrice with PBS buffer (pH 7.4). Subsequently, fresh medium containing AuNRs@SiO$_2$-CAA (150 µg mL^{-1}) was added, and the cells were further incubated for 9 h before PA imaging. Subsequently, NaOCl (ranging from 0 to 20 µM) was added to the aforementioned culture dishes and equilibrated for 30 s for additional PA imaging.

Specificity Verification: To verify the specificity of AuNRs@SiO$_2$-CAA, various ROS were prepared, including NaOCl, peroxynitrite ($ONOO^-$), H_2O_2, singlet oxygen ($^1O_2$), hydroxyl radical (•OH), and superoxide (•O_2^-). NaOCl, $ONOO^-$, and H_2O_2 were prepared by diluting the original solutions with water. $^1O_2$ was generated by mixing NaOCl and H_2O_2. •OH was obtained through the Fenton reaction by combining $Fe(NH_4)_2(SO_4)_2\cdot 6H_2O$ with H_2O_2, with final concentrations calculated based on Fe^{2+}. •O_2^- was prepared by dissolving potassium superoxide (KO_2) in DMSO. Subsequently, different ROS (35 µM) were added to PBS (pH 7.4) containing AuNRs@SiO$_2$-CAA (150 µg mL^{-1}), separately. UV–vis absorption spectra were measured from 400 to 1000 nm. PA signals were detected from 680 to 900 nm using the MSOT InVision 256-TF Scanner.

Cell Viability: RAW264.7 cells were seeded in a 96-well plate at a density of 5000 cells per well and cultured overnight. Subsequently, fresh DMEM medium containing varying concentrations of AuNRs@SiO$_2$-CAA (0 − 400 µg mL^{-1}) was added to replace the previous medium, and cells were further incubated for 24 or 48 h. Cell viability was quantitatively analyzed using the MTT assay.

Cellular Uptake: The cellular uptake of AuNRs@SiO$_2$-CAA was analyzed using flow cytometry and confocal microscopy. For flow cytometry, RAW264.7 and CT26 cells were seeded in 24-well plates (1×10^5 cells per well) and cultured overnight. RhB-labeled AuNRs@SiO$_2$-CAA were added to the seeded RAW264.7 or CT26 cells at a final concentration of 150 µg mL^{-1}. Following incubation for various time points (0, 0.5, 3, 6, 6.5, 7, 8, 9, 12, and 24 h), the cells were washed three times with PBS, collected, and subjected to flow cytometry analysis.

For confocal imaging, RAW264.7 and CT26 cells were seeded on glass coverslips in 24-well plates (1×10^5 cells per well) and incubated overnight. The cells were incubated with RhB-labeled AuNRs@SiO_2-CAA (150 µg mL^{-1}) for various durations (0, 0.5, 3, 6, 6.5, 7, 8, 9, 12, and 24 h). After washing three times with PBS buffer to remove excess RhB-labeled AuNRs@SiO_2-CAA, the cells were subjected to confocal imaging. The excitation wavelength was 555 nm using the red channel.

Photothermal Performance: Solutions containing 150 µg mL^{-1} of AuNRs, AuNRs@SiO_2, and AuNRs@SiO_2-CAA were irradiated with a laser (808 nm, 1.25 W cm^{-2}) for 8 min. PTI were recorded at 2-min intervals using an infrared thermal imaging camera (FLIR), and the temperatures were transformed accordingly.

To verify the effect of laser density on photothermal efficiency, solutions containing 150 µg mL^{-1} of AuNRs, AuNRs@SiO_2, and AuNRs@SiO_2-CAA were irradiated with lasers of different densities (0.25, 0.5, 1, 1.25, 1.5 W cm^{-2}) for 8 min, and PTI were recorded.

The photostability of AuNRs@SiO_2-CAA was tested under 808 nm laser on/off cyclic irradiation. Specifically, AuNRs@SiO_2-CAA solutions were irradiated for 8 min (laser on), followed by natural cooling for 15 min (laser off). This on/off cycle was repeated four times, and the temperature of the solution was measured every 30 sec.

Animal Experiments: All animal experiments were conducted following the institutional guidelines for animal experimentation using the animal-use protocols approved by The University of Queensland's Animal Ethics Committee (2021/AE001029). The method for validating the detection capability of AuNRs@SiO_2-CAA for subcutaneous HOCl was as follows: Female BALB/c mice ($n = 4$) were subcutaneously injected with AuNRs@SiO_2-CAA (1.5 mg mL^{-1}, 100 µL) and HOCl (100 µM, 100 µL) sequentially into the right hind leg. Mice injected only with AuNRs@SiO_2-CAA (1.5 mg mL^{-1}, 100 µL) served as positive controls ($n = 4$). PA images and signal intensities at 680 and 820 nm were recorded using the MSOT InVision 256-TF Scanner at 5-min intervals.

AuNRs@SiO_2-CAA was utilized for HOCl imaging in both inflammation and tumor models. The back inflammation model was established by subcutaneously injecting LPS (1 µg mL^{-1}, 100 µL) into the back of female BALB/c mice ($n = 4$). AuNRs@SiO_2-CAA (1.5 mg mL^{-1}, 100 µL) was injected into the same location 4 h post-LPS injection. PA images and signal intensities were recorded at 5-min intervals. The tumor-bearing mouse model was created by subcutaneously injecting CT26 cells (50 µL, 1×10^7 cells mL^{-1}) into female BALB/c mice ($n = 4$). When the tumor volume reached 100 mm^3, AuNRs@SiO_2-CAA (1.5 mg mL^{-1}, 100 µL) was injected around the tumor. PA images and signal intensities of these mice were recorded at 0, 10, 20, 120, 240, and 360 min.

To validate the biodistribution of intravenously injected AuNRs@SiO_2-CAA, RhB-labelled AuNRs@SiO_2-CAA (10 mg kg^{-1}) were intravenously injected into CT26 tumor-bearing mice ($n = 8$). FL imaging was conducted using the IVIS optical imaging system at 0, 2, 4, 6, 12, 24, 36, 48, and 72 h post-injection. Mice were euthanized at 6, 12, 24, and 72 h post-injection, and major organs and tumors were collected for ex vivo imaging.

For in vivo photothermal imaging, PBS, AuNRs@SiO_2, and AuNRs@SiO_2-CAA (10 mg kg^{-1}) were intravenously injected into CT26 tumor-bearing mice ($n = 4$ per group). 12 h post-injection, each group was subjected to laser irradiation (808 nm, 1.25 W cm^{-2}, 6 min). PTI were recorded using FLIR every 2 min, and the temperatures were converted accordingly.

The procedure for tumor detection, PTT, and inflammation monitoring during PTT using AuNRs@SiO_2-CAA in tumor-bearing mice was as follows:

Experimental groups setup: When the tumor volume of CT26 tumor-bearing mice reached 100 mm^3 (approximately 7 days post-cell injection, designated as day 0), the mice were randomly divided into five groups ($n = 4$ per group): PBS, AuNRs@SiO_2, AuNRs@SiO_2-CAA, AuNRs@SiO_2 + Laser, and AuNRs@SiO_2-CAA + Laser.

Injections and treatments: PBS, AuNRs@SiO_2, and AuNRs@SiO_2-CAA dispersed in PBS were intravenously injected into the mice on day 0. Laser irradiation (808 nm, 1.25 W cm^{-2}, 6 min) was performed on the groups requiring laser irradiation 12 h post-injection. Mice were intravenously injected for the second time on day 3.

Monitoring and data collection: PA images and signal intensities at 680 and 820 nm were recorded at 0, 6, 12, 24, and 48 h post both injections. Weight and tumor volume of all mice were recorded every 3 d. Tumor volume was calculated using the formula: $\text{Volume} = \text{Length} \times \text{Width}^2 \times 0.5$.

Endpoint analysis: After 3 weeks, euthanasia was performed on all mice to collect tumors and major organs (heart, liver, spleen, lungs, and kidneys), followed by further slicing for H&E staining.

Statistical Analysis: All the experiments were performed in triplicate with the data presented as mean ± SEM (standard error of the mean) using GraphPad Prism.

Supporting Information

Supporting Information is available from the Wiley Online Library or from the author.

Acknowledgements

The authors gratefully acknowledge the financial support from the National Health and Medical Research Council (APP1175808). H.Z. wishes to acknowledge the UQ-CSC PhD scholarship. Assistance of Australian Microscopy & Microanalysis Research Facility at the Centre for Microscopy and Microanalysis (CMM) and Queensland Node of the Australian National Fabrication Facility (ANFF-Q), the University of Queensland, were also acknowledged.

Conflict of Interest

The authors declare no conflict of interest.

Author Contributions

H.Z. and R.Z. conceived the original concept, initiated the project, and designed the research. H.Z., M.W., M.A., and Z.Z. carried out the synthesis and characterization of the nanoprobe. H.Z., M.W., and F.A.N.S. performed the biological investigations. Q.M. and C.F. performed the molecule synthesis and characterization. R.Z., Z.P.X, and H.T.T. supervised the project. H.Z. and R.Z. analyzed and discussed the data and wrote the manuscript. All authors provided feedback and approved the final version of the manuscript.

Data Availability Statement

The data that support the findings of this study are available from the corresponding author upon reasonable request.

Keywords

cancer, hypochlorous acid, inflammation, photoacoustic imaging, photothermal therapy, theranostic nanoprobe

Received: August 13, 2024
Revised: October 8, 2024
Published online: October 23, 2024

---

[1] M. Naghavi, K. L. Ong, A. Aali, H. S. Ababneh, Y. H. Abate, C. Abbafati, R. Abbasgholizadeh, M. Abbasian, M. Abbasi-Kangevari,

H. Abbastabar, S. Abd ElHafeez, M. Abdelmasseh, S. Abd-Elsalam, A. Abdelwahab, M. Abdollahi, M.-A. Abdollahifar, M. Abdoun, D. M. Abdulah, A. Abdullahi, M. Abebe, S. S. Abebe, A. Abedi, K. H. Abegaz, E. S. Abhilash, H. Abidi, O. Abiodun, R. G. Aboagye, H. Abolhassani, M. Abolmaali, M. Abouzid, et al., *Lancet* **2024**, *403*, 2100.

[2] a) I. B. Belyaev, I. V. Zelepukin, P. A. Kotelnikova, G. V. Tikhonowski, A. A. Popov, A. Y. Kapitannikova, J. Barman, A. N. Kopylov, D. N. Bratashov, E. S. Prikhozhdenko, A. V. Kabashin, S. M. Deyev, A. V. Zvyagin, *Adv. Sci.* **2024**, *11*, 2307060; b) J. Chen, R. Chen, C. V. Chau, A. C. Sedgwick, Q. Xue, T. Chen, S. Zeng, N. Chen, K. K. Y. Wong, L. Song, Y. Ren, J. Yang, J. L. Sessler, C. Liu, *J. Am. Chem. Soc.* **2024**, *146*, 4620; c) B. Sridharan, H. G. Lim, *J. Nanobiotechnol.* **2023**, *21*, 437; d) A. Zare, P. Shamshiripour, S. Lotfi, M. Shahin, V. F. Rad, A. R. Moradi, F. Hajiahmadi, D. Ahmadvand, *J. Controlled Release* **2022**, *351*, 805; e) L. Lin, L. V. Wang, *Nat. Rev. Clin. Oncol.* **2022**, *19*, 365.

[3] a) Y. Zeng, T. Dou, L. Ma, J. Ma, *Adv. Sci.* **2022**, *9*, 2202384; b) C. Moore, J. V. Jokerst, *Theranostics* **2019**, *9*, 1550; c) B. Park, D. Oh, J. Kim, C. Kim, *Nano Converg.* **2023**, *10*, 29; d) X. Ai, Z. Wang, H. Cheong, Y. Wang, R. Zhang, J. Lin, Y. Zheng, M. Gao, B. Xing, *Nat. Commun.* **2019**, *10*, 1087.

[4] Q. Meng, M. Wu, Z. Shang, Z. Zhang, R. Zhang, *Coord. Chem. Rev.* **2022**, *457*, 214398.

[5] J. T. Lang, D. Kulkarni, C. W. Foster, Y. Huang, M. A. Sepe, S. Shimpalee, D. Y. Parkinson, I. V. Zenyuk, *Chem. Rev.* **2023**, *123*, 9880.

[6] N. Renaudin, C. Demené, A. Dizeux, N. Ialy-Radio, S. Pezet, M. Tanter, *Nat. Methods* **2022**, *19*, 1004.

[7] a) X. Meng, X. Pang, K. Zhang, C. Gong, J. Yang, H. Dong, X. Zhang, *Small* **2022**, *18*, 2202035; b) L. Zhang, L. Zhang, X. Zhang, Y. Zhao, S. Fang, J. You, L. Chen, *TrAC Trend Anal. Chem.* **2023**, *169*, 117377.

[8] L. Z. Zhao, W. Yuan, J. Y. Li, L. Q. Yang, Y. Q. Su, J. J. Peng, R. Chen, H. P. Tham, H. Z. Chen, W. Q. Lim, H. J. Xiang, P. Y. Xing, F. Y. Li, Y. L. Zhao, *Adv. Funct. Mater.* **2018**, *28*, 1806162.

[9] a) N. Li, X. Li, J. Li, Y. Li, T. Zhang, *Anal. Chem.* **2024**, *96*, 7342; b) Y. Zhao, L. Li, Q. Ye, Y. Gong, R. Yang, H. Liu, *Anal. Chem.* **2023**, *95*, 14043; c) Y.-Y. Zhao, X. Zhang, Z. Chen, Y. Xu, H. Kim, H. Jeong, Y. R. Lee, J. Lee, X. Li, J. Yoon, *Aggregate* **2024**, *5*, e514.

[10] a) R. Vankayala, K. C. Hwang, *Adv. Mater.* **2018**, *30*, 1706320; b) Y. Lai, Y. Dang, F. Li, C. Ding, H. Yu, W. Zhang, Z. Xu, *Adv. Funct. Mater.* **2022**, *32*, 2200016; c) X. Yang, T. Yang, Q. Liu, X. Zhang, X. Yu, R. T. K. Kwok, L. Hai, P. Zhang, B. Z. Tang, L. Cai, P. Gong, *Adv. Funct. Mater.* **2022**, *32*, 2206346; d) Y. Ma, S. Gou, Z. Zhu, J. Sun, M.-A. Shahbazi, T. Si, C. Xu, J. Ru, X. Shi, R. L. Reis, S. C. Kundu, B. Ke, G. Nie, B. Xiao, *Adv. Mater.* **2024**, *36*, 2309516.

[11] P. Manivasagan, T. Thambi, A. Joe, H.-W. Han, S.-H. Seo, Y. Jun Jeon, J. Conde, E.-S. Jang, *Prog. Mater. Sci.* **2024**, *144*, 101292.

[12] a) D. Zhang, J. Yang, S. Ye, Y. Wang, C. Liu, Q. Zhang, R. Liu, *Small* **2022**, *18*, 2107071; b) L. Li, X. Liang, T. He, X. Li, X. Huang, N. Wang, M. Shen, Y. Shu, R. Wu, M. Zhang, Q. Wu, C. Gong, *Biomaterials* **2022**, *290*, 121815.

[13] J. Checa, J. M Aran, *J. Inflamm. Res.* **2020**, *13*, 1057.

[14] a) L. Y. Yang, Q. Luo, L. Lu, W. W. Zhu, H. T. Sun, R. Wei, Z. F. Lin, X. Y. Wang, C. Q. Wang, M. Lu, H. L. Jia, J. H. Chen, J. B. Zhang, L. X. Qin, *J. Hematol. Oncol.* **2020**, *13*, 3; b) J. A.-O. Albrengues, M. A.-O. Shields, D. Ng, C. A.-O. Park, A. A.-O. Ambrico, M. A.-O. X. Poindexter, P. A.-O. Upadhyay, D. A.-O. Uyeminami, A. A.-O. Pommier, V. Küttner, E. A.-O. Bružas, L. A.-O. Maiorino, C. A.-O. Bautista, E. M. Carmona, P. A. Gimotty, D. A.-O. Fearon, K. A.-O. Chang, S. A.-O. Lyons, K. A.-O. Pinkerton, L. C. Trotman, M. A.-O. Goldberg, J. A.-O. X. Yeh, M. A.-O. Egeblad, *Science* **2018**, *361*, eaao4227; c) G. Wang, J. Yan, H. Tian, B. Li, X. Yu, Y. Feng, W. Li, S. Zhou, Y. Dai, *Adv. Mater.* **2024**, *36*, 2312588.

[15] a) M. Aioub, S. R. Panikkanvalappil, M. A. El-Sayed, *ACS Nano* **2017**, *11*, 579; b) S. Wang, J. Huang, H. Zhu, J. Zhu, Z. Wang, Y. Xing, X. Xie, K. Cai, J. Zhang, *Adv. Funct. Mater.* **2023**, *33*, 2213151; c) J. Xie, R. Dong, T. Zhang, F. Guo, H. Li, X. Chen, Y. Wu, X. Zhang, Y. Yong, Z. Gu, *Chem. Eng. J.* **2024**, *490*, 151756.

[16] D. Wu, L. Chen, Q. Xu, X. Chen, J. Yoon, *Acc. Chem. Res.* **2019**, *52*, 2158.

[17] P. Valadez-Cosmes, S. Raftopoulou, Z. N. Mihalic, G. Marsche, J. Kargl, *Pharmacol. Ther.* **2022**, *236*, 108052.

[18] Q. Zhang, X. Hu, X. Dai, P. Ling, J. Sun, H. Chen, F. Gao, *ACS Nano* **2021**, *15*, 13633.

[19] a) F. Zhang, X. Liang, W. Zhang, Y.-L. Wang, H. Wang, Y. H. Mohammed, B. Song, R. Zhang, J. Yuan, *Biosens. Bioelectron.* **2017**, *87*, 1005; b) M. M. Fortibui, C. Park, N. Y. Kim, T. H. Kim, M. H. Lee, *Anal. Chem.* **2024**, *96*, 9408.

[20] a) Z. Ye, M. Ji, K. Wu, J. Yang, A. A. Liu, W. Sun, D. Ding, D. Liu, *Angew. Chem., Int. Ed.* **2022**, *61*, 202204518; b) L. Gui, J. Yan, J. Zhao, S. Wang, Y. Ji, J. Liu, J. Wu, K. Yuan, H. Liu, D. Deng, Z. Yuan, *Biosens. Bioelectron.* **2023**, *240*, 115660.

[21] X. B. Wang, H. J. Li, Q. Li, Y. Ding, C. Hu, Y. C. Wu, *J. Hazard. Mater.* **2022**, *427*, 127874.

[22] a) A. Sharma, P. Verwilst, M. Li, D. Ma, N. Singh, J. Yoo, Y. Kim, Y. Yang, J.-H. Zhu, H. Huang, X.-L. Hu, X.-P. He, L. Zeng, T. D. James, X. Peng, J. L. Sessler, J. S. Kim, *Chem. Rev.* **2024**, *124*, 2699; b) W. Gu, S. Li, Y. Yang, S. Wang, K. Li, Y. Zhao, J. Mu, X. Chen, *TrAC* **2023**, *169*, 117360.

[23] L. Yao, C. Yin, F. Huo, *Micromachines* **2022**, *13*, 1328.

[24] T. Huang, H. Ji, S. Yan, Y. Zuo, J. Li, J. W. Y. Lam, C. Han, B. Z. Tang, *Biomaterials* **2023**, *297*, 122108.

[25] L. J. Palmer, P. R. Cooper, M. R. Ling, H. J. Wright, A. Huissoon, I. L. Chapple, *Clin. Exp. Immunol.* **2012**, *167*, 261.

[26] a) F. Brøndsted, Y. Fang, L. Li, X. Zhou, S. Grant, C. I. Stains, *Chemistry* **2024**, *30*, 202303038; b) L. Yuan, W. Lin, Y. Yang, H. Chen, *J. Am. Chem. Soc.* **2012**, *134*, 1200.

[27] a) G. Gao, X. Sun, G. Liang, *Adv. Funct. Mater.* **2021**, *31*, 2100738; b) L. Yao, D. Bojic, M. Liu, *J. Pharm. Anal.* **2023**, *13*, 960.

[28] J. Lu, Z. Li, X. Zheng, J. Tan, Z. Ji, Z. Sun, J. You, *J. Mater. Chem. B.* **2020**, *8*, 9343.

[29] Y. Liu, M. Yang, J. Zhang, X. Zhi, C. Li, C. Zhang, F. Pan, K. Wang, Y. Yang, J. Martinez de la Fuentea, D. Cui, *ACS Nano* **2016**, *10*, 2375.

[30] C. Chan, W. Zhang, Z. Xue, Y. Fang, F. Qiu, J. Pan, J. Tian, *Anal. Chem.* **2022**, *94*, 5918.

[31] a) J. Lan, L. Chen, Z. Li, L. Liu, R. Zeng, Y. He, Y. Shen, T. Zhang, Y. Ding, *Adv. Healthcare Mater.* **2024**, 2400046; b) D. Zhu, Y. Lu, S. Yang, T. Hu, C. Tan, R. Liang, Y. Wang, *Adv. Sci.* **2024**, *11*, 2401064.